Crustal structure beneath the Qilian Orogen Zone from multiscale seismic tomography

Biao Guo*, **JiuHui Chen, QiYuan Liu, and ShunCheng Li**

State Key Laboratory of Earthquake Dynamics, Institute of Geology, China Earthquake Administration, Beijing 100029, China

Abstract: The Qilian Orogen Zone (QOZ), located in the north margin of the Tibetan Plateau, is the key area for understanding the deformation and dynamics process of Tibet. Numerous geological and geophysical studies have been carried out on the mechanics of the Tibetan Plateau deformation and uplift; however, the detailed structure and deformation style of the Qilian Orogen Zone have remained uncertain due to poor geophysical data coverage and limited resolution power of inversion algorithms. In this study, we analyze the P-wave velocity structure beneath the Qilian Orogen Zone, obtained by applying multi-scale seismic tomography technique to P-wave arrival time data recorded by regional seismic networks. The seismic tomography algorithm used in this study employs sparsity constraints on the wavelet representation of the velocity model via L1-norm regularization. This algorithm can deal efficiently with uneven-sampled volumes, and can obtain multi-scale images of the velocity model. Our results can be summarized as follows: (1) The crustal velocity structure is strongly inhomogeneous and consistent with the surface geological setting. Significant low-velocity anomalies exist in the crust of northeastern Tibet, and slight high-velocity anomalies exist beneath the Qaidam Basin and Alxa terrane. (2) The Qilian Orogen Zone can be divided into two main parts by the Laji Shan Faults: the northwestern part with a low-velocity feature, and the southeastern part with a high-velocity feature at the upper and middle crust. (3) Our tomographic images suggest that northwestern and southeastern Qilian Orogen Zones have undergone different tectonic processes. In the northwest Qilian Orogen Zone, the deformation and growth of the Northern Tibetan Plateau has extended to the Heli Shan and Beida Shan region by northward over-thrusting at the upper crust and thickening in the lower crust. We speculate that in the southeast Qilian Orogen Zone the deformation and growth of the Northern Tibet Plateau were of strike-slip style at the upper crust; in the lower crust, the evidence suggests ductile shear extrusion style and active frontage extension to the Alxa terrane. (4) The multi-scale seismic tomography technique provides multi-scale analysis and sparse constraints, which has allowed to us obtain stable, high-resolution results.

Keywords: Qilian Orogen Zone; crustal structure; multi-scale seismic tomography

1. Introduction

The Qilian Orogen Zone (QOZ), a typical continent-continent collisional orogeny, located in the northern margin of the Tibetan Plateau, has an excellent record of early to middle Paleozoic subduction–accretion that resulted from convergence between the Alxa terrane and Qaidam blocks (Xiao WJ et al., 2009). This region is crucial for understanding the Tibet dynamics process.

The QOZ is thought to be a result of the closure of the Proto-Tethyan Ocean. It appears to have undergone a long-term, complicated and multistage continental collisional process between various accretionary continental terranes (Gehrels et al., 2011; Wu YB and Zheng YF, 2013; Cheng F et al., 2015). The ophiolite belts and ultrahigh-pressure metamorphic rocks found here have recorded the evolutionary history of the Tibetan Plateau (Yin and Harrison, 2000; Meyer et al., 1998; Xiao WJ et al., 2009; Song SG et al.,

2013). The tectonic evolution of the QOZ can be divided into the following stages: (1) an opening along the North Qilian Ocean in the Neoproterozoic to early-middle Cambrian, (2) closure of archipelago ocean basins during the late Cambrian-Middle Ordovician, and (3) collisional and intra-continental orogeny in the middle Cenozoic, due to shortening and uplift of the Tibet Plateau (Song SG et al., 2013).

In the Cenozoic, northward bulldozer-like compression of the Indian Plate has driven movement and rotation along the Altyn-Tagh Fault, reshaping topographic and tectonic patterns of the Qilian and adjacent regions (Song SG et al., 2013). Global Positioning System (GPS) results show that the QOZ undergoes active northeastern shortening at a rate of 13 mm/a. The velocities of the displacement rapidly decrease from the northern Qaidam Basin to the Hexi Corridor. From the Altyn Tagh Range to the southeastern Qilian Shan, the velocities of the displacement significantly increase, and the direction of the displacement gradually changes from NE to SE (Yin and Harrison, 2000; Zhang PZ et al., 2004). This feature implies that large amounts of crustal shortening and eastward extrusion are occurring within the Qilian Orogen Zone. Hundreds of kilometers of offset along the left-lateral Altyn-Tagh Fault

have been absorbed within the Qilian Orogen Zone and partly accommodated by NE-directed crustal shortening (Cheng F et al., 2015). A large amount of this displacement has been transferred further east through crustal transposition within the QOZ. Finally, this eastward extrusion of crustal material from the QOZ is a possible driving mechanism for (a) sinistral strike-slip faulting along the Haiyuan and West Qinling Faults (Burchfiel et al., 1991; Duvall et al., 2011), (b) crustal thickening in the Qinling region, and (c) anticlockwise rotation of the Ordos block (Zhang GB et al., 2008), leading to (d) extension into the adjacent North China block graben systems, such as the Weihe Graben (Meyer et al., 1998; Cheng F et al., 2015; Sun WJ et al., 2015).

Furthermore, the QOZ has experienced a complicated evolutionary history; evidence of multiple collisions preserved in and around the QOZ has been the focus of many investigations. The QOZ's deformation style has important implications for how Cenozoic shortening and eastern extrusion induced by the Indo-Asia collision has been accommodated across the plateau (England and Houseman, 1986; Burchfiel et al., 1989; Tapponnier et al., 2001; Wang YD et al., 2011, Zuza et al., 2016). Despite its essential tectonic position, the QOZ has not been subjected to thorough geophysical examination, leaving many important problems unresolved. In particular, all of the following remain highly uncertain: the collision behavior between the QOZ and the Alxa terrane; the boundaries between geological units; the style of deformation in this zone; and the northeastern extrusion into the Qilian range.

In recent years, many studies based on geophysical and geological data have been conducted; they have established the general tectonic evolution frames for the QOZ and its adjacent areas, and its preliminary crustal and lithospheric structure model (Wang P and Wang ZG, 1997; Xiao WJ et al., 2009; Gehrels et al., 2003, 2011; Chen JH, 2005; Guo B et al., 2004; Song SG et al., 2013; Wang Q et al., 2013, 2016; Guo B et al., 2004; Gao X et al., 2018; Bao XW et al., 2013; Cheng F et al., 2015; Feng M et al., 2014; Chen M et al., 2017; Tian XB et al., 2013; Yi GX et al., 2008; Guo XY et al., 2016; Shi JY et al., 2017; Zou CQ et al., 2017). However, due to lack of high-quality geophysical data and/or a suitable inversion technique, those studies focused primarily on linear seismic profiles (Feng M et al., 2014; Guo XY et al., 2016; Shi JY et al., 2017; Zhang ZJ et al., 2013) or on the low-resolution lithospheric mantle structure (Li C et al., 2008; Shi JY et al., 2017; Zhang Q et al., 2011; Yue H et al., 2012; Huang ZX, 2003; Li L et al., 2013; Sun WJ et al., 2015; Chen M et al., 2017). Therefore, high-resolution 3-D crustal structure imaging beneath the QOZ is still critically needed to answer the questions mentioned above.

In this study, we conducted local multi-scale seismic tomography in the QOZ and adjacent area using high-quality arrival-time data of local earthquakes recorded by regional seismic networks. By integrating our tomographic images and related research results, we provide a high-resolution crustal P-wave structure, establish a dynamic evolution model, and attempt to answer the question of deformation and extrusion style.
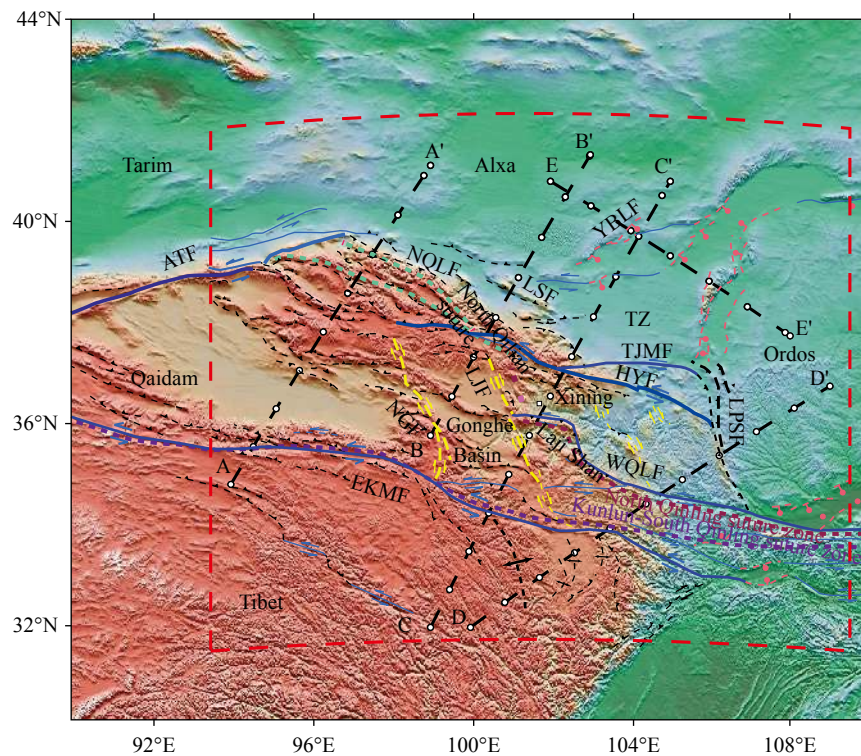

Figure 1. Geological sketch map of the Qilian Orogen System. The rectangle denotes the study area. The black dot lines denote profile location; the distance between the white dots is 1 degree. Colored lines denote main faults. ATF: Altyn Tagh Fault, HYF: Haiyuan Fault, EKMF: Eastern Kunlun Mountains Fault, TJMF: Tianjing Mountain Fault, NQLF: North Qilian Fault, WQLF: West Qiling Fault, NGF: Ngola Shan Fault, LJF: Laji Shan Fault, NWQO: Northwestern Qilian Orogen, and SEQO: Southeastern Qilian Orogen. NWA: Northwestern Alxa, SEA: Southeastern Alxa, TZ: Transition Zone between Tibet, Alxa, Ordos. The faults data are from Zuza et al. (2016).

2. Tectonic Settings and Travel Time Data

The Qilian Orogen Zone is part of the Qinling-Qilian-Kunlun Fold System, located in a joint region among the Alxa terrane in the north, the Tarim Craton in the northwest, and the Ordos Block in the northeast (see Figure 1). It is more than 300 km wide and about 1000 km long, striking in the SE direction, and has an average elevation of 3000–5000 m. Geographically the QOZ is defined by the North Qilian faults, Heli Shan faults, and Longshoushan faults system in the northeast; the Kunlun faults system in the southwest; and the Altyn-Tagh faults system in the west (Song SG et al., 2013; Zhang JX et al., 2015). The study area generally involves four main tectonic units called the Alxa Terrane (AT), the North Qilian Orogen belt (NQOZ), the Qilian block (QB), and the Qaidam Basin (QDB); they are near parallel and nearly E–W trending, and bounded from north to south by the North and South Qilian suture zones. To the north, the AT is an ancient and stable craton, located in the western margin of the North China Block. The NQOZ is an imbricate thrust belt of Precambrian basement overlain by Paleozoic sedimentary sequences. The QB consists of Precambrian basement with characteristic 900–100 Ma plutonic rocks (Yin A and Harrison, 2000; Wu C et al., 2016). To the south, the QDB is a Mesozoic intra-continental basin with a sedimentary sequence that varies in thickness from ~5 km near the margins to ~15 km in the center (Wang YD et al., 2012).

In this study, we collect Pg and Pn arrival time data from local earthquakes recorded by regional seismic networks in the Qilian Orogen Zone and its adjacent areas. The arrival time data are from the database of the China Earthquake Data Center, collected during 2009–2015.

The travel time data used in this study were selected carefully based on the following criteria: (1) All the seismic hypocentres and seismic stations are distributed in 32°N–44°N and 94°E–108°E. (2) Each event was recorded by more than 6 seismic stations, and a minimum of 10 Pg or Pn phases were picked. (3) The uncertainty of hypocentral locations is not more than ~5 km. (4) The travel time residuals based on the CRUST1.0 velocity model are less than 5.0 s. (Exceptions: To make the events distribution more uniform, some events recorded by fewer than 6 seismic stations in the low seismicity areas, such as inner Tibet, where the seismicity is very low, were also selected).

The data used in this study are a total of 64828 travel time picks of Pn and Pg waves of 6898 earthquakes, selected from data collected at 76 seismic stations. Figure 2 shows the hypocentres distribution of the 6898 chosen events and the 76 seismic stations used in this study. As shown in Figure 2, most of the seismic stations are distributed in the west part of the study area, and in the depth range of the events was 5–20 km, which implied that the detailed structure of the QOZ could be well recovered.

The abundance of secondary P wave arrivals (i.e. Pn phases) in our catalogs, at epicenter distances ranging from 180 to 500 km, considerably increases the sampling rays in the lower crust and the top of the upper mantle, and improves the precision of epicenter depth location. Although few events occurred in the lower crust and no event occurred in the uppermost mantle, numerous rays from Pn waves sampled the lower crust and upper mantle. Generally, most raw picks are closely clustered along the apparent travel time curves (Figure 3). However, some outliers and misidentifications are still present and will be sorted out in subsequent pro-
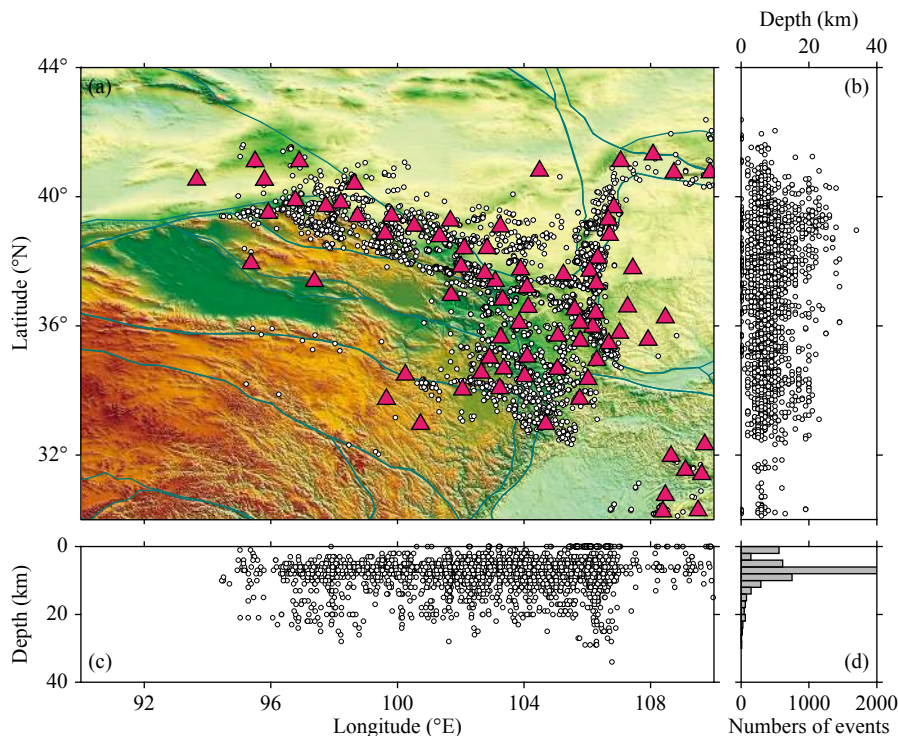

Figure 2. Map view of stations and local events. The red triangles represent seismic stations used in this study. The black circles denote events. Figures 2b–2c represent the distribution of events on the vertical section. Figure 2d is the histogram for statistics of earthquake depth vs. number of events.
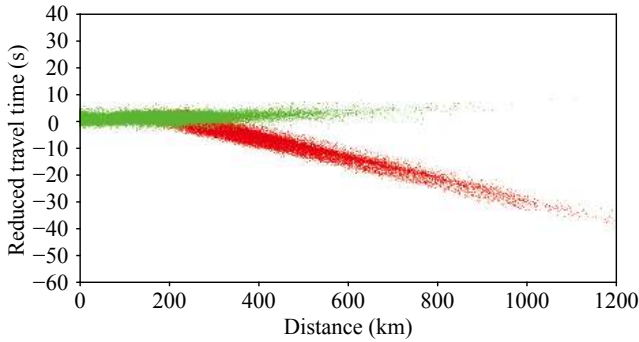
Figure 3. Traveltime curves. The green dots denote Pg phase; the red dots denote Pn phase. This figure shows average Pg and Pn wave velocities. The reduced travel time was calculated based on the average crustal velocity of 6.35 km/s.

cessing (relocation), based on selection criterion (4).

3. Methodology

In this study, we applied the multi-scale tomographic method to our data set to image the 3-D P-wave velocity structure of the crust and upper mantle under the QOZ. The standard approach to local seismic tomography is first to start with an estimated optimal 1-D crustal model and then apply simultaneous inversion of the hypocentre and a crustal model such as VELEST (Kissling et al., 1994). However, due to the existence in this study area of strong lateral variations in the crustal structure, strong fluctuations of topography, and particularly low-velocity sediments between its mountains, the optimal 1-D model is not a suitable choice as an initial model for tomographic inversion. The 3-D CRUST1.0 model (Laske et al., 2013) was therefore used as the initial velocity model. A fine grid of 25 km×25 km×10 km in the Cartesian domain was used to parameterize the study region. The earthquakes location and tomographic inversion algorithm developed by Gao X et al. (2018) was used in this study. This software package adapts a layered fast marching method for forward problems (Rawlinson and Sambridge, 2004); it was designed to handle multi-arrivals in a strong inhomogeneous layered 3-D medium. The velocity model is parametrized in terms of homogeneous velocity grids and employs a cubic spline as the interpolation function. We transform the model parameters from the spatial domain to the wavelet domain using D4 wavelet. Based on the sparse assumption, a Gradient Projection for Sparse Reconstruction (GPSR) technique (Figueiredo et al., 2007) is used for the tomography inversion. The GPSR algorithm adopts bound-constrained quadratic programming (BCQP) to formulate the mix quadratic error term and a sparseness-constrain regularization term. Computational experiments show that GPSR approaches perform well in a wide range of applications, often being significantly faster than competing methods (Figueiredo et al., 2007). Subsequently, hypocentres are relocated in the updated velocity model. The earthquakes are relocated using a global grids searching method based on the travel time field. This software has been successfully applied to several projects (Li Z et al., 2015; Gao X et al., 2018).

3.1 Multi-scale Seismic Tomography

A simplified description of the seismic tomography algorithm is given below. In general, seismic travel-time tomography involves solving the system of linear equations

$$d = Gm, \qquad (1)$$

where d is the data vector (travel time residuals), m is the model parameter vector (velocity perturbations), and G is the Gram matrix. Moreover, the model parameter vector m can be transformed from the spatial domain into the wavelet domain via the equation

$$\tilde{m} = Wm, \qquad (2)$$

where W is the 3-D wavelet-transform operator. In this study, our model parameter vector is expanded at grid nodes in terms of the Daubechies D4 transform (Daubechies, 1992). Then one can have

$$d = GW^{-1}Wm = GW^{-1}\tilde{m} = \tilde{G}\tilde{m}, \qquad (3)$$

and

$$\tilde{G} = GW^{-1}, \qquad (4)$$

where W^{-1} is the inverse transformation of the operator W.

Thus, our inverse problem is recast as seeking the coefficients of the wavelet basis functions $\tilde{m}$. Since the wavelet-based matrix of model parameters is usually sparse, the inverse problem comes down to minimizing the mixed l_2-l_1 functional of the form

$$F = \left\| \tilde{G}\tilde{m} - d \right\|_2^2 + 2\lambda \|\tilde{m}\|_1 \qquad (5)$$

where λ is a sparse constraint factor.

For actual observations, an uneven distribution of sources and seismic stations leads to uneven ray path sampling in the study volume. It is self-evident that uneven ray path sampling leads to different resolving power in different parts of the volume of interest. Usually, some spatial smoothing factor, or simply parameterization coarsening, has been employed to deal with such ill-conditioned data sets. Traditionally, these forms of "regularization" have been applied uniformly across the entire model, which raises the possibility that, while the ill-constrained regions are being damped, the well-constrained regions are being over-smoothed – hence information may be lost (Chiao LY and Kuo BY, 2001). In this study, we have chosen parametrization of the 3-D model in the wavelet domain, which results in multi-scale resolution throughout the volume, i.e., different regions have different degrees of resolution.

3.2 Resolution Test

We perform checkerboard testing to evaluate the resolution of our tomographic images. In this test, we set up a checkerboard velocity model by adding ±5.0 percent velocity variation to the initial model and generating synthetic P-wave travel times from each earthquake hypocentre to the recording stations. Before the inversion, we add Gaussian distributed noise with a standard deviation of 0.1 s, with zero mean, to the synthetic travel times. Finally, the synthetic data are inverted using the same parametrization, constraints, and control parameters used in the real data inversion (Figure 4). Two input models with different scale anomalies are tested and plotted on horizontal sections at depths of 10, 25, and 40 km respectively. The checkerboard tests with 50 km anomalies are shown in Figures 4a–4c; the checkerboard tests with 75
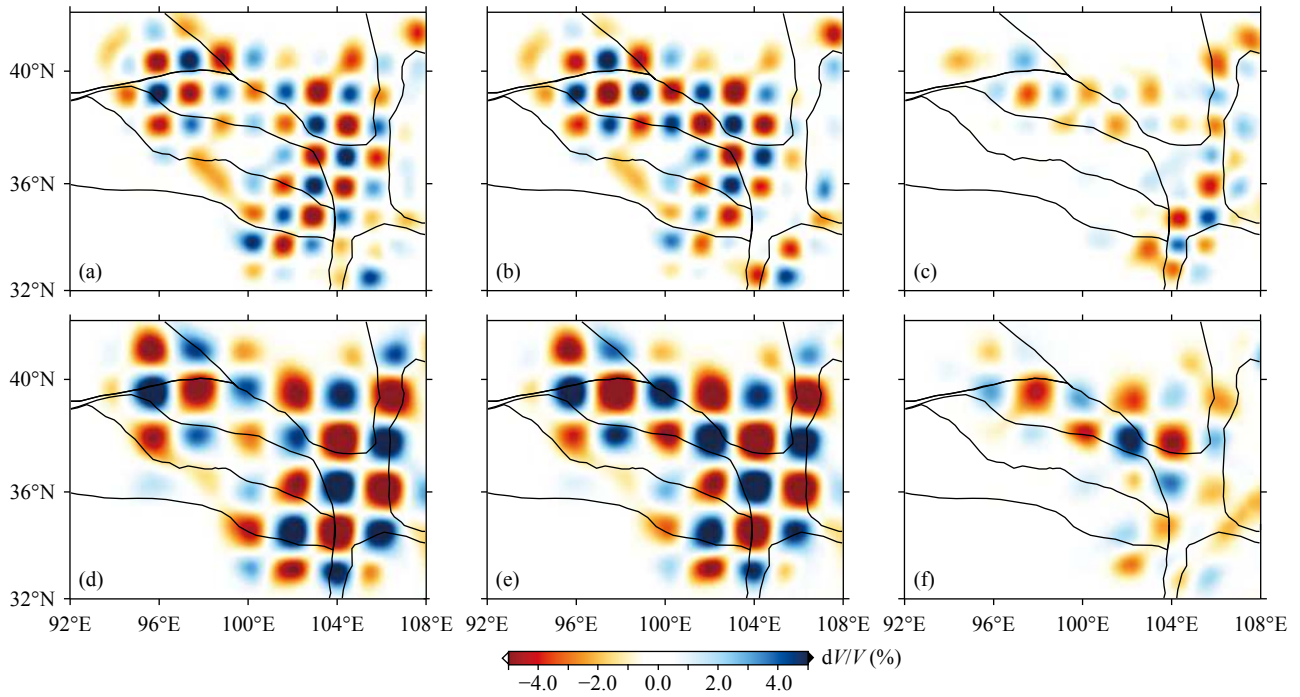
Figure 4. Checkerboard resolution test. The block lines denote faults. The input anomaly scale is 50 km in Figures 4a–4c and 75 km in Figures 4d–4f. At depth 40 km, only the region around QOZ can be well recovered.

km anomalies are shown in Figures 4d–4f. Checkerboard test results show that most of the anomalies of 75 km can be well recovered. In the QOZ and to the east of the study region, at depths of 10–40 km, the perturbations are well restored, indicating that tomography images in this region are reliable. However, near the margin of our study area, especially at the lower crust and upper mantle depth beneath the southern and southeastern QOZ, the checkerboard feature is not well recovered; this could be a consequence of smearing along the direction of ray because of poor rays crossing.

4. Results and Discussion
We performed three iterations of our inversions, the travel time RMS value being reduced from 0.869 s for the starting model to

0.676 s in the final tomography model and relocation.

4.1 Horizontal Velocity Variation and Block Structure
Figure 5 shows the P-wave velocity tomography images at three different depths, together with large historical earthquakes around each layer and the major active faults. Strong lateral velocity variations are visible in the crust and upper mantle in the study area, and the velocity distribution characteristics are consistent with the surface geological features. In general, low-velocity anomalies are visible in northern Tibet, and high-velocity anomalies are visible in the Alxa terrane, Ordos block, Yangze craton, and transition zone (TZ) between Tibet and Ordos. In addition, the epicenters of the large historical earthquakes are generally located at the boundary zone where P-wave velocity changes drastically in a short distance (Figures 5a–5c).
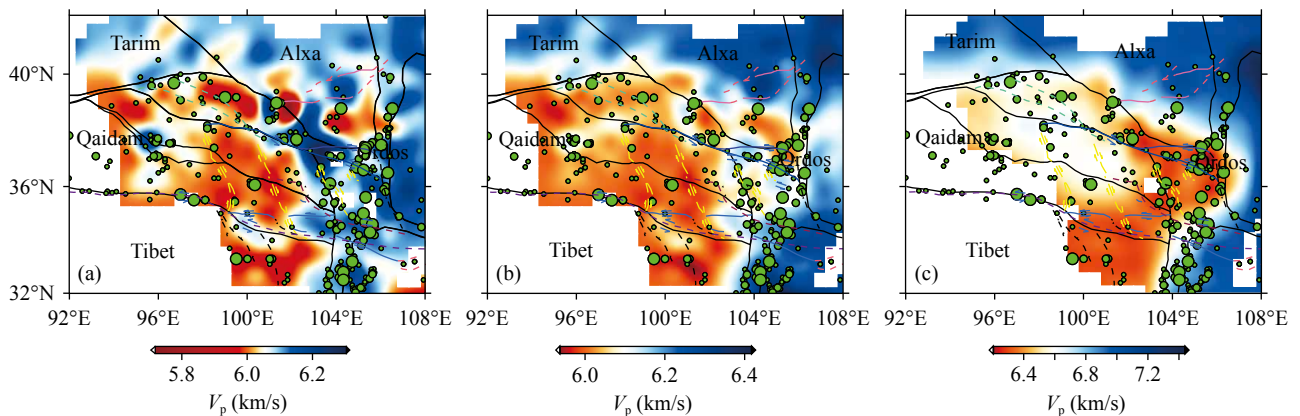

Figure 5. Horizontal sections of P-wave velocity at the depths of 10 km (a), 25 km (b), and 40 km (c), respectively. The green circles represent historic earthquakes (magnitude>6.0); black line indicates major faults.

Guo B et al.: Crustal structure of Qilian Orogen

The velocity slice at the 10 km depth (Figure 5a) represents the P-wave velocity structure at the upper crust. As Figure 5a shows, obvious low-velocity anomalies appear in the QOZ west Qinling block, especially in the northwestern Qilian. The north Qaidam Basin has a slight high-velocity feature, consistent with characteristics of the North Qaidam Ultra-High-Pressure Metamorphic Belt (UHPMB). The QOZ divides into two parts at intersection of the Yumushan Mountain and the ERF: the northwestern part (WQOZ) with low-velocity features, and the southeastern part (EQOZ) with high-velocity features. Prominent high-velocity anomalies are visible at upper-crust depth beneath the Ordos, the Yangze, and the transition zone (TZ) between Tibet and Ordos.

The P-wave velocity slice at the 20 km depth (Figure 5b) represents the P-wave velocity structure at the middle crust. As Figure 5b shows, Qilian, Songpan-Garzê, and West Qinling Terranes have an obvious low-velocity feature at middle crust depths. The UHPMB also shows slight high-velocity features. The WQOZ displays similar features as those at upper crust; however, low-velocity anomalies exist at the conjunction between eastern and western North Qilian Orogen, extending in the SE-NW direction. This feature implies the existence of channels for material transportation. The low-velocity anomalies extrude under the Hexi corridor and reach to Beida Shan, Heli Shan, and Longshoushan.

From Figures 5a–5b, the west Alxa (WAX) shows a relatively homogeneous structure, but the eastern Alxa block (EAX) has a very complex structure. At the EAX, many ductile shear faults are distributed, implying EAX had a weak crust and underwent strong deformation. At the TZ, relatively high-velocity anomalies are featured in the upper crust and complex structure is seen in the middle and low crust; these observations are consistent with the results from Cheng B et al. (2014), and imply a weak or ductile lower crust. At the Yumushan and Longshoushan regions, low-velocity anomalies intrude into the Alxa terrane.

The velocity slice at 40 km depth (Figure 5c) mainly reflects the velocity distribution characteristics of the lower crust. As Figure 5c shows, a prominent feature in this image is the pronounced relatively high-velocity of the southern and central Qilian Orogen and strong low-velocity of the eastern margin of Tibet. The Alxa, Ordos, and Yangze show very high-velocity anomalies. This feature implies that the ductile low crustal has extended to the TZ and EAX, reaching to the southwestern margin of the Ordos block.

It is notable that the WQOZ and EQOZ show different velocity distribution patterns, and the velocity beneath the WQOZ is lower than the velocity of the EQOZ. These features are consistent with the results from ambient noise tomography (Li HY et al., 2013; Bao XW et al., 2013), and gravity inversion (Li HL et al., 2017). In the WQOZ, the magnetic anomalies are 50–200 nT greater than in the EQOZ, where the ophiolites in this region are mainly distributed (Xiong XQ et al., 2016). The WQOZ and EQOZ have distinctly different geological characteristics: Paleozoic magmatic rocks are widely distributed in the WQOZ but not in the EQOZ, and the WQOZ has relatively high heat flow value (Wang Y, 2001; Li HY et al., 2013). The WQOZ is characterized by a thick crust (about 60–70 km), and its Moho is deeper than it is in the EQOZ (Li HY et al., 2014; Zheng D et al., 2016). Receiver function results have re-

vealed that there is a ~10 km difference in the Moho depth between the WQOZ and EQOZ (Yue H et al., 2012; Bao XW et al., 2013). Beneath the northwestern Qilian Orogen, the average crust thickness is about 60–65 km. Lower densities (less than 2.6 g/cm^3) are also found in the WQOZ (Li HL et al., 2017). On the average, the crustal thickness changes from 62 km in the WQOZ to 38 km in the EQOZ (Bao XW et al., 2013; Cheng B et al., 2014). These differences are indicative of a thick, hotter, and weaker crust beneath the WQOZ. In contrast, the EQOZ has an average Moho depth of approximately 50 km and a relative high-velocity crust. GPS data show that the strain rate within the WQOZ is an order of magnitude smaller than the rate within the EQOZ (Gan WJ et al., 2007; Liang SM et al., 2013). Moreover, weak anisotropy with fast polarization is present nearly along the N-S direction in the WQOZ, while the EQOZ shows relative strong anisotropy with EW direction polarization (Becker et al., 2012; Wu CL et al., 2015). These features imply that the deformation style changes from pure shear in the WQOZ to left-lateral shear in the EQOZ (Chang LJ et al., 2017).

The Yabulaishan Mountain divides the Alxa into two parts: the northwestern Alxa (WAX) has high-velocity, homogeneous, and stable features, which are generally considered to be evidence that they are older, colder, and mechanically stronger; the southeastern Alxa (EAX) is dominated by very complex and relative low-velocity features, which developed a ductile shear zone (Wang P and Wang ZG, 1997), indicating a mechanically weak upper and middle crust, and is generally considered to be characteristics of soft and easy to be deformed. These features correlate strongly to the distribution of crustal thickness from receiver function studies (Yue H et al., 2012; Zheng D et al., 2016). The lower crustal flow model for eastern Tibet, after Royden et al. (1997) and Clark and Royden (2000), shows flow lines around the Eastern Himalayan syntaxis and around the stable Sichuan basin, and a branch of flow extending to the TZ and the EAX.

4.2 Vertical Velocity Variation Along Profiles

Figure 6 presents vertical cross-sections of the P-wave velocity images from the surface down to 70 km depth along five profiles, as shown in Figure 1. The major faults are marked on the top of profiles; Moho depth data are derived from CRUST1.0 (Laske et al., 2013). In general, prominent low-velocity anomalies are visible beneath the Tibet, relatively high-velocity anomalies are found beneath the Alxa terranes in the upper and middle crust, and the Hexi corridor shows high-velocity in the upper and middle crust. The transition zone between the Ordos block and the Tibetan Plateau shows a very complex structure in the upper and middle crust.

In Figure 6a, Profile AA' is located in the west part of the study area, starting from the Qaidam Basin and extending SW to NE across the NWQLF and NQLF to the Alxa terrane. The north margin of the Qaidam UHPMB shows slight high-velocity anomalies. A clear boundary is present between Qaidam and southern Qilian and suggests that the north margin Qaidam fault (NQDF) cuts the whole crust. This feature further suggests that the south Qilian block subducted southward at a steep angle, and is consistent with the northward convergence between the Oulongbuluk and
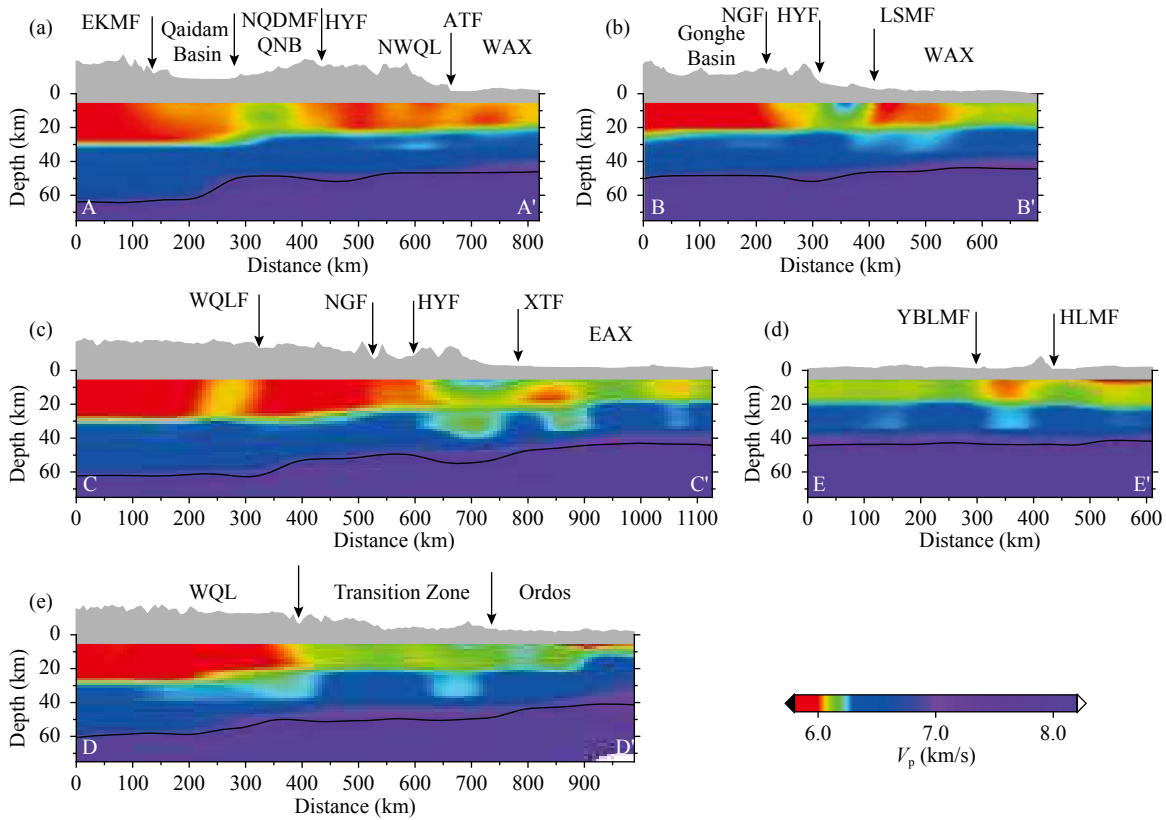
Figure 6. Tomographic P-wave velocity structure along five vertical profiles. The black arrows on the top of image indicate location of faults. Black lines represent Moho taken from CRUST1.0. Note: locations of profiles are plotted on Figure 1; topography is plotted above each profile (gray filled area).

the Qaidam basin (Sun WJ et al., 2015). Gehrels et al. (2003) argued that southward subduction occurred along the northeastern margin of Qaidam Basin, and the magmatism produced the plutons.

Profile BB′ crosses the Qilian Orogen, Longshoushan Mountain, and the Alxa terrane. The Gonghe basin shows a low-velocity feature in the upper and middle crust. Prominent upper crustal high-velocity anomalies are found beneath the Hexi corridor and Longshoushan. Clear crustal scale boundaries exist at both sides of the Hexi corridor. The large and deep boundary at Longshoushan suggests that the Altyn-Tagh Fault extends to this region.

Profile CC′, starting from the Songpan Terrane and crossing the Qilian Orogen to the Alxa terrane, is similar to Profile BB′. The upper and middle crust show low-velocity features in the region south of the Haiyuan Fault, and slightly high-velocity anomalies with a southward dipping feature are observed beneath the WQLF. The south margin of the Alxa has a high-velocity feature in the crust that extends southward.

In Profiles BB′ and CC′, the dipping imbricate faults at the boundary and high-velocity feature in the upper crust suggest that the Hexi corridor is an old and cold micro-block. The Heli Shan Fault and Longshoushan Fault marks the northernmost boundary of the Qilian Orogen (Figures 5b–5c), suggesting that the northernmost active front of the Tibet extends to the Heli Shan Fault and Longshoushan Fault (Zheng WJ et al., 2013). As shown by Figures

7a–7b, the foreland basin of the Hexi Corridor is of the tectonically "piggy-back" type; the present-day deformation front of the Tibetan Plateau might have migrated into the Alxa ~2 Ma ago (Zheng WJ et al., 2013). Obvious high-velocity anomalies exist in the upper crust beneath the Hexi corridor near Longshoushan, perhaps reflecting the remnants of the Proto-Tethys oceanic slab in that area. Another clear high-velocity anomaly beneath the Alxa block extends from the middle crust to the Hexi corridor's lower crust and upper mantle at a sharp angle, its upper part possibly overthrusts onto the Alxa.

The profile DD′ starts from Tibet, crosses the transition zone, and reaches the Ordos Block. Prominent upper and middle crustal low-velocity anomalies exist beneath the Tibet, and the Ordos block and the TZ have a relatively thin crust and high-velocity feature in their upper and middle crust. Clear boundaries exist among the TZ, the Tibetan plateau, and the Ordos block. The southwestern part of the Ordos Basin is characterized by a high-velocity feature and its western boundary is marked by the Guyuan–Longshoushan Fault.

Along the western part of the Qilian Orogen frontal thrust system, the surface topography and Moho display mirror images; the steep elevation and bend-down-like Moho reveal vertical thickening and the "pure-shear" mode of crustal deformation (England and Houseman, 1986; Chang LJ et al., 2017); these observations are consistent with crustal deformation characteristic of young orogen sandwiched between strong tectonic blocks (Shi JY et al.,
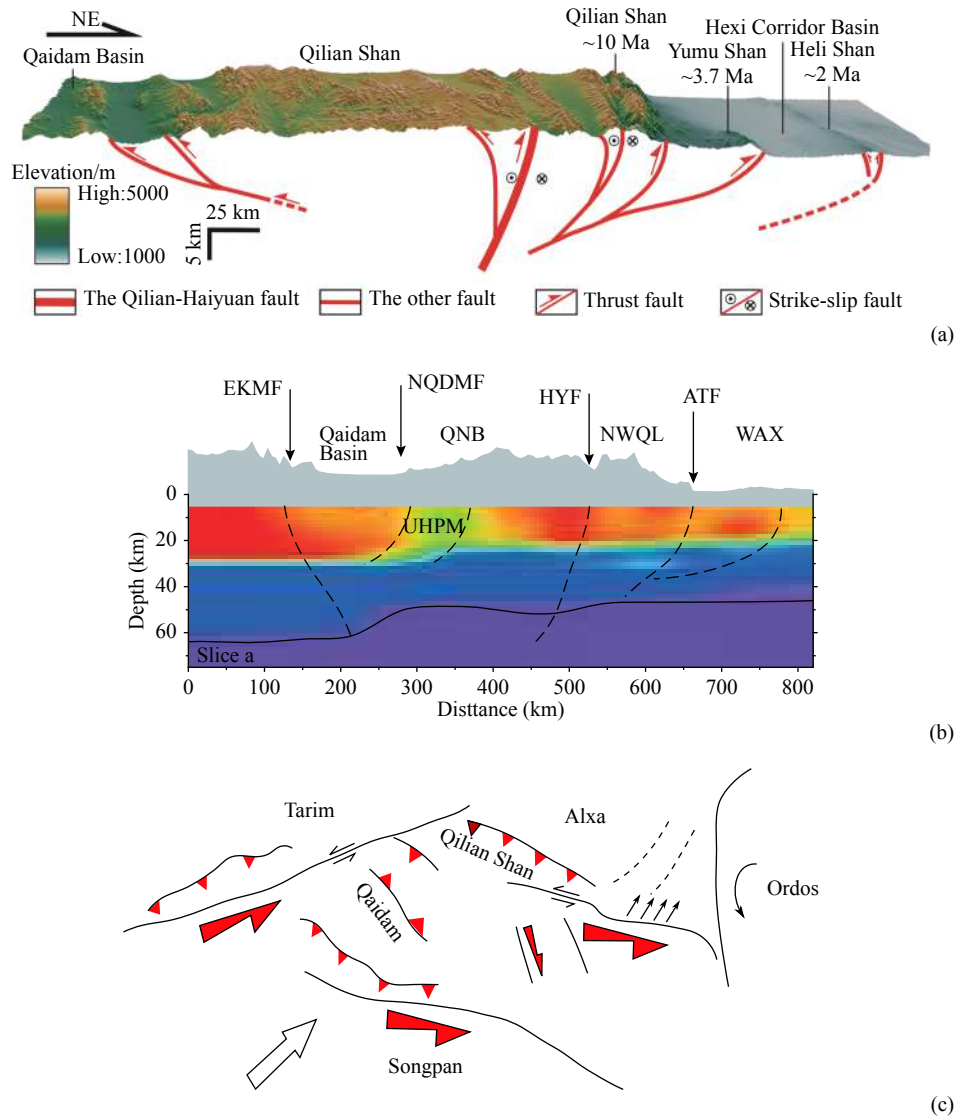
Figure 7. Schematic diagram of the Qilian Orogen Zone's tectonic geometry and kinematic growth. (a) shows a model of tectonic deformation of the Qilian Shan (Zheng WJ et al., 2013), (b) shows tomography section along profile a, (c) cartoon of kinematic growth of the Qilian Orogen Zone (modified from Métivier et al., 1998). The black solid lines denote boundary faults; the arrows denote direction of movement.

2017; Zheng D et al., 2016). The eastern part of the Qilian is dominated by strike-slip and ductile shear crustal deformation (Tapponnier et al., 1982; Chang LJ et al., 2017); the development of the topography and Moho implies the deformation beneath Qilian gently propagate to the Alxa.

Based on the conjugate fault model proposed by Zhang J et al. (2007), this study gives a more detailed dynamic model, as shown by Figure 7, than the simplified cartoon explanation for the growth of the Tibetan Plateau. The north-northeastward growth of the Tibetan Plateau propagates along the Altyn-Tagh Fault, because of the block of the Alxa terrane, formed imbricated and nappe thrusts and northward overturned folds at northwestern Qilian orogen zone, thickening at lower crust, and the foreland basin of the Hexi Corridor becomes a tectonically "piggy-back" basin, which implies present-day deformational front of the Tibetan Plateau might have migrated into the Alxa (Zheng WJ et al., 2013). Because of the weak crust of the eastern Alxa, the

Gonghe basin and Yumushan region, the deformation partitioned into left-lateral strike slip along the Haiyuan Fault (Meyer et al., 1998; Métivier et al., 1998; Zheng WJ et al., 2013), and the displacement direction turn from NNE ward to NEE ward.

5. Conclusions

In this paper, we present a model of the crustal P-wave velocity structure beneath the Qilian Orogen Zone in high-resolution 3-D, based on a multi-scale seismic tomography algorithm that we have applied to local travel time data from 76 seismic stations of the Chinese Provincial Seismic Networks. The tomographic results show that the northwestern QOZ exhibits a low-velocity feature, and the southeastern QOZ has a high-velocity feature where results from receiver function imaging reveal a deeper Moho depth than the in surrounding areas. The Gonghe basin between the Ngola Fault and Laji Faults appears to be a mechanical transition zone, which is characterized by a relatively low-velocity zone, and

divides the Qilian Orogen into two mechanically distinct tectonic blocks: the northwestern and southeastern Qilian Orogen Zones (NWQOZ and SEQOZ). Our results demonstrate different crustal structures, crustal thicknesses, and deformation styles in the two tectonic units. These observations provide new evidence regarding the mode of deformation across the Qilian Orogen. We argue that the different mechanisms between the northwestern and southeastern Qilian Orogen Zones give important new insight into the deformation style and dynamical transposition in the northeastern Tibetan Plateau. Based on previously published results and our new tomographic images, we speculate that as the Indian Plate continues its northward movement and is blocked by the mechanically strong crust of the western Alxa, the crust of the western Qilian Orogen Zone has thickened by over-thrusting. At the SEQOZ, the deformation style transforms from pure NNE directional thrust to NEE directional strike-slip features. A series of strike-slip features in the upper crust accommodate tectonic escape through ductile shear in the middle and lower crust. Because of mechanical weakness of the lower crust of the eastern Alxa, the deformation will propagate from the boundaries to the Alxa and Ordos, and result in the rotation of these blocks. Apparently, since the closure of the Proto-Tethyan Ocean, these two parts of the QOZ have undergone distinct evolutional histories (i.e. crustal tectonic shortening processes and ductile shear extrusion processes). Our results provide critical geophysical constraints for the Qilian Orogan Zone, reconcile its surface geology and crustal structure, and help explain dynamical models of its tectonic shortening and escape.

Acknowledgments

References

Bao, X. W., Song, X. D., Xu, M. J., Wang, L. S., Sun, X. X., Mi, N., Yu, D. Y., and Li, H. (2013). Crust and upper mantle structure of the North China Craton and the NE Tibetan Plateau and its tectonic implications. *Earth Planet. Sci. Lett.*, *369–370*, 129–137. https://doi.org/10.1016/j.epsl.2013.03.015

Becker, T. W., Lebedev, S., and Long, M. D. (2012). On the relationship between azimuthal anisotropy from shear wave splitting and surface wave tomography. *J. Geophys. Res.*, *117*(B1), B01306. https://doi.org/10.1029/2011JB008705

Burchfiel, B. C., Molnar, P., Zhao, Z. Y., Liang, K. Y., Wang, S. J., Huang, M. M., Sutter, J. (1989). Geology of the Ulugh Muztagh area, northern Tibet. *Earth Planet. Sci. Lett.*, *94*(1-2), 57–70. https://doi.org/10.1016/0012-821X(89)90083-6

Burchfiel, B. C., Zhang, P. Z., Wang, Y. P., Zhang, W. Q., Song, F. M., Deng, Q. D., Molnar, P., and Royden, L. (1991). Geology of the Haiyuan fault zone, Ningxia-Hui Autonomous Region, China, and its relation to the evolution of the northeastern margin of the Tibetan Plateau. *Tectonics*, *10*(6), 1091–1110. https://doi.org/10.1029/90TC02685

Chang, L. J., Ding, Z. F., Wang, C. Y., and Flesch, L. M. (2017). Vertical coherence of deformation in lithosphere in the NE margin of the Tibetan plateau using GPS and shear-wave splitting data. *Tectonophysics*, *699*, 93–101. https://doi.org/10.1016/j.tecto.2017.01.025

Chen, J. H., Liu, Q. Y., Li, S. C., Guo, B., and Lai, Y. G. (2005). Crust and upper mantle S-wave velocity structure across Northeastern Tibetan Plateau and Ordos block. *Chinese J. Geophys.*, *48*(2), 369–379. https://doi.org/10.1002/cjg2.663

Chen, M., Niu, F. L., Tromp, J., Lenardic, A., Lee, C. T. A., Cao, W. R., and Ribeiro, J. (2017). Lithospheric foundering and underthrusting imaged beneath Tibet. *Nat. Commun.*, *8*, 15659. https://doi.org/10.1038/ncomms15659

Cheng, B., Cheng, S. Y., Zhang, G. W., and Zhao, D. P. (2014). Seismic structure of the Helan–Liupan–Ordos western margin tectonic belt in North-Central China and its geodynamic implications. *J. Asian Earth Sci.*, *87*, 141–156. https://doi.org/10.1016/j.jseaes.2014.01.006

Cheng, F., Jolivet, M., Dupont-Nivet, G., Wang, L., Yu, X. J., and Guo, Z. J. (2015). Lateral extrusion along the Altyn Tagh Fault, Qilian Shan (NE Tibet): insight from a 3D crustal budget. *Terra Nova*, *27*(6), 416–425. https://doi.org/10.1111/ter.12173

Chiao, L. Y., and Kuo, B. Y. (2001). Multiscale seismic tomography. *Geophys. J. Int.*, *145*(2), 517–527. https://doi.org/10.1046/j.0956-540x.2001.01403.x

Clark, M. K., and Royden, L. H. (2000). Topographic ooze: Building the eastern margin of Tibet by lower crustal flow. *Geology*, *28*(8), 703–706. https://doi.org/10.1130/0091-7613(2000)28<703:TOBTEM>2.0.CO;2

Daubechies, I. (1992). *Ten Lectures on Wavelets*. Philadelphia: Society for Industrial and Applied Mathematics.

Duvall, A. R., Clark, M. K., van der Pluijm, B. A., and Li, C. Y. (2011). Direct dating of Eocene reverse faulting in northeastern Tibet using Ar-dating of fault clays and low-temperature thermochronometry. *Earth Planet. Sci. Lett.*, *304*(3–4), 520–526. https://doi.org/10.1016/j.epsl.2011.02.028

England, P., and Houseman, G. (1986). Finite strain calculations of continental deformation: 2. Comparison with the India-Asia collision zone. *J. Geophys. Res. Solid Earth*, *91*(B3), 3664–3676. https://doi.org/10.1029/JB091iB03p03664

Feng, M., Kumar, P., Mechie, J., Zhao, W., Kind, R., Su, H., Xue, G., Shi, D., and Qian, H. (2014). Structure of the crust and mantle down to 700 km depth beneath the East Qaidam basin and Qilian Shan from P and S receiver functions. *Geophys. J. Int.*, *199*(3), 1416–1429. https://doi.org/10.1093/gji/ggu335

Figueiredo, M. A. T., Nowak, R. D., and Wright, S. J. (2007). Gradient projection for sparse reconstruction: application to compressed sensing and other inverse problems. *IEEE J. Sel. Top. Signal Process.*, *1*(4), 586–597. https://doi.org/10.1109/JSTSP.2007.910281

Gan, W. J., Zhang, P. Z., Shen, Z. K., Niu, Z. J., Wang, M., Wan, Y. G., Zhou, D. M., and Cheng, J. (2007). Present-day crustal motion within the Tibetan Plateau inferred from GPS measurements. *J. Geophys. Res. Solid Earth*, *112*(B8), B08416. https://doi.org/10.1029/2005JB004120

Gao, X., Gao, B., Chen, J. H., Liu, Q. Y., Li, S. C., and Li, Y. (2018). Rebuilding of the lithosphere beneath the western margin of Ordos: Evidence from multiscale seismic tomography. *Chinese J. Geophys.* (in Chinese), *61*(7), 2736–2749. https://doi.org/10.6038/cjg2018L0319

Gehrels, G., Kapp, P., DeCelles, P., Pullen, A., Blakey, R., Weislogel, A., Ding, L., Guynn, J., Martin, A., … Yin, A. (2011). Detrital zircon geochronology of pre-Tertiary strata in the Tibetan-Himalayan orogen. *Tectonics*, *30*(5), TC5016. https://doi.org/10.1029/2011tc002868

Gehrels, G. E., Yin, A., and Wang, X. F. (2003). Detrital-zircon geochronology of the northeastern Tibetan plateau. *Geol. Soc. Am. Bull.*, *115*(7), 881–896. https://doi.org/10.1130/0016-7606(2003)115<0881:DGOTNT>2.0.CO;2

Guo, B., Liu, Q. Y., Chen, J. H., Zhao, D. P., Li, S. C., and Lai, Y. G. (2004). Seismic tomographic imaging of the crust and upper mantle beneath the Northeastern edge of the Qinghai-Xizang plateau and the Ordos area. *Chinese J. Geophys.* (in Chinese), *47*(5), 790–797. https://doi.org/10.3321/j.issn:0001-5733.2004.05.009

Guo, X. Y., Gao, R., Li, S. Z., Xu, X., Huang, X. F., Wang, H. Y., Li, W. H., Zhao, S. J., and Li, X. Y. (2016). Lithospheric architecture and deformation of NE Tibet: New insights on the interplay of regional tectonic processes. *Earth Planet.*

Sci. Lett., *449*, 89–95. https://doi.org/10.1016/j.epsl.2016.05.045

Huang, Z. X., Su, W., Peng, Y. J., Zheng, Y. J., and Li, H. Y. (2003). Rayleigh wave tomography of China and adjacent regions. *J. Geophys. Res.*, *108*(B2), 2073. https://doi.org/10.1029/2001JB001696

Kissling, E., Ellsworth, W. L., Eberhart-Phillips, D., and Kradolfer, U. (1994). Initial reference models in local earthquake tomography. *J. Geophys. Res. Solid Earth*, *99*(B10), 19635–19646. https://doi.org/10.1029/93JB03138

Laske, G., Masters., G., Ma, Z. T., and Pasyanos, M. (2013). Update on CRUST1.0 - A 1-degree Global Model of Earth's Crust. In *Geophysical Research Abstracts, vol. 15, Abstract EGU2013-2658*. Vienna: EGU.

Li, C., van der Hilst, D. R., Meltzer, A. S., and Engdahl, E. R. (2008). Subduction of the Indian lithosphere beneath the Tibetan Plateau and Burma. *Earth Planet. Sci. Lett.*, *274*(1–2), 157–168. https://doi.org/10.1016/j.epsl.2008.07.016

Li, H. L., Fang, J., and Braitenberg, C. (2017). Lithosphere density structure beneath the eastern margin of the Tibetan Plateau and its surrounding areas derived from GOCE gradients data. *Geod. Geodyn.*, *8*(3), 147–154. https://doi.org/10.1016/j.geog.2017.02.007

Li, H. Y., Shen, Y, Huang, Z. X., Li, X. F., Gong, M., Shi, D. N., Sandvol, E., and Li, A. B. (2014). The distribution of the mid-to-lower crustal low-velocity zone beneath the northeastern Tibetan Plateau revealed from ambient noise tomography. *J. Geophys. Res. Solid Earth*, *119*(3), 1954–1970. https://doi.org/10.1002/2013JB010374

Li, L., Li, A. B., Shen, Y., Sandvol, E. A., Shi, D. N., Li, H. Y., and Li, X. F. (2013). Shear wave structure in the northeastern Tibetan Plateau from Rayleigh wave tomography. *J. Geophys. Res. Solid Earth*, *118*(8), 4170–4183. https://doi.org/10.1002/jgrb.50292

Li, Z., Guo, B., Chen, J. H., Liu, Q. Y. (2015). Parameterization in seismic tomography. *Progress in Geophysics* (*in Chinese*), *30*(4), 1616–1624. https://doi.org/10.6038/pg20150416

Liang, S. M., Gan, W. J., Shen, C. Z., Xiao, G. R., Liu, J., Chen, W. T., Ding, X. G., and Zhou, D. M. (2013). Three-dimensional velocity field of present-day crustal motion of the Tibetan Plateau derived from GPS measurements. *J. Geophys. Res. Solid Earth*, *118*(10), 5722–5732. https://doi.org/10.1002/2013JB010503

Métivier, F., Gaudemer, Y., Tapponnier, P., and Meyer, B. (1998). Northeastward growth of the Tibet plateau deduced from balanced reconstruction of two depositional areas: The Qaidam and Hexi Corridor basins, China. *Tectonics*, *17*(6), 823–842. https://doi.org/10.1029/98TC02764

Meyer, B., Tapponnier, P., Bourjot, L., Métivier, F., Gaudemer, Y., Peltzer, G., Guo, S. M., and Chen, Z. T. (1998). Crustal thickening in Gansu-Qinghai, lithospheric mantle subduction, and oblique, strike-slip controlled growth of the Tibet plateau. *Geophys. J. Int.*, *135*(1), 1–47. https://doi.org/10.1046/j.1365-246X.1998.00567.x

Rawlinson, N., and Sambridge, M. (2004). Wave front evolution in strongly heterogeneous layered media using the fast marching method. *Geophys. J. Int.*, *156*(3), 631–647. https://doi.org/10.1111/j.1365-246X.2004.02153.x

Royden, L.H., Burchfiel B. C., King R. W., Wang E., Chen Z. L., Shen F., Liu Y. P. (1997). Surface deformation and lower crustal flow in Eastern Tibet. *Science*, *276*, 788–790. https://doi.org/10.1126/science.276.5313.788

Shi, J. Y., Shi, D. N., Shen, Y., Zhao, W. J., Xue, G. Q., Su, H. P., and Song, Y. (2017). Growth of the northeastern margin of the Tibetan Plateau by squeezing up of the crust at the boundaries. *Sci. Rep.*, *7*, 10591. https://doi.org/10.1038/s41598-017-09640-0

Song, S. G., Niu, Y. L., Li, S., and Xia, X. H. (2013). Tectonics of the North Qilian orogen, NW China. *Gondw. Res.*, *23*(4), 1378–1401. https://doi.org/10.1016/j.gr.2012.02.004

Sun, W. J., Li, S. Z., Liu, X., Santosh, M., Zhao, S. J., Guo, L. L., Cao, H. H., Yu, S., Dai, L. M., and Zhang, Y. (2015). Deep structures and surface boundaries among Proto-Tethyan micro-blocks: Constraints from seismic tomography and aeromagnetic anomalies in the Central China Orogen. *Tectonophysics*, *659*, 109–121. https://doi.org/10.1016/j.tecto.2015.07.033

Tapponnier, P., Xu, Z. Q., Roger, F., Meyer, B., Arnaud, N., Arnaud, G., and Yang, J. S. (2001). Oblique stepwise rise and growth of the Tibet Plateau. *Science*, *294*(5547), 1671–1677. https://doi.org/10.1126/science.105978

Tapponnier P., Peltzer G., Le Dain A. Y., Armijo R., Cobbold P. (1982). Propagating extrusion tectonics in Asia; new insights from simple experiments with plasticine. *Geology*, *10*, 611–616.

Tian, X. B., and Zhang, Z. J. (2013). Bulk crustal properties in NE Tibet and their implications for deformation model. *Gondw Res.*, *24*(2), 548–559. https://doi.org/10.1016/j.gr.2012.12.024

Wang, P., and Wang, Z. G. (1997). Division of the Alxa Block and its attribution. *Earthquake* (*in Chinese*), *17*(1), 103–112.

Wang, Q., Gao, Y., Shi, Y. T., and Wu, J. (2013). Seismic anisotropy in the uppermost mantle beneath the northeastern margin of Qinghai-Tibet plateau: evidence from shear wave splitting of SKS, PKS and SKKS. *Chinese J. Geophys.* (*in Chinese*), *56*(3), 892–905. https://doi.org/10.6038/cjg20130318

Wang, Q., Niu, F. L., Gao, Y., and Chen, Y. T. (2016). Crustal structure and deformation beneath the NE margin of the Tibetan plateau constrained by teleseismic receiver function data. *Geophys. J. Int.*, *204*(1), 167–179. https://doi.org/10.1093/gji/ggv420

Wang, Y. (2001). Heat flow pattern and lateral variations of lithosphere strength in China mainland: Constraints on active deformation. *Phys. Earth Planet. Inter.*, *126*(3–4), 121–146. https://doi.org/10.1016/S0031-9201(01)00251-5

Wang, Y. D., Zheng, J. J., Zhang, W. L., Li, S. Y., Liu, X. W., Yang, X., and Liu, Y. H. (2012). Cenozoic uplift of the Tibetan Plateau: Evidence from the tectonic-sedimentary evolution of the western Qaidam Basin. *Geosci. Front.*, *3*(2), 175–187. https://doi.org/10.1016/j.gsf.2011.11.005

Wu, C., Yin, A., Zuza, V. A., Zhang, J. Y., Liu, W. C., and Ding, L. (2016). Pre-Cenozoic geologic history of the central and northern Tibetan Plateau and the role of Wilson cycles in constructing the Tethyan orogenic system. *Lithosphere*, *8*(3), 254–292. https://doi.org/10.1130/L494.1

Wu, C. L., Xu, T., Badal, J., Wu, Z. B., and Teng, J. W. (2015). Seismic anisotropy across the Kunlun fault and their implications for northward transforming lithospheric deformation in northeastern Tibet. *Tectonophysics*, *659*, 91–101. https://doi.org/10.1016/j.tecto.2015.07.030

Wu, Y. B., and Zheng, Y. F. (2013). Tectonic evolution of a composite collision orogen: an overview on the Qinling–Tongbai–Hong'an–Dabie–Sulu orogenic belt in central China. *Gondw. Res.*, *23*(4), 1402–1428. https://doi.org/10.1016/j.gr.2012.09.007

Xiao, W. J., Windley, B. F., Yong, Y., Yan, Z., Yuan, C., Liu, C. Z., and Li, J. L. (2009). Early Paleozoic to Devonian multiple-accretionary model for the Qilian Shan, NW China. *J. Asian Earth Sci.*, *35*(3–4), 323–333. https://doi.org/10.1016/j.jseaes.2008.10.001

Xiong, S. Q., Yang, H., Ding, Y. Y., Li, Z. K., and Li, W. (2016). Distribution of igneous rocks in China revealed by aeromagnetic data. *J. Asian Earth Sci.*, *129*, 231–242. https://doi.org/10.1016/j.Jseaes.2016.08.016

Yi, G. X., Yao, H. J., Zhu, J. S., and van der Hilst, R. D. (2008). Rayleigh-wave phase velocity distribution in China continent and its adjacent regions. *Chinese J. Geophys.*, *51*(2), 265–274. https://doi.org/10.1002/cjg2.1218

Yin, A., and Harrison, T. M. (2000). Geologic evolution of the Himalayan-Tibetan orogen. *Annu. Rev. Earth Planet. Sci.*, *28*, 211–280. https://doi.org/10.1146/annurev.earth.28.1.211

Yue, H., Chen, J. J., Sandvol, E., Ni, J., Hearn, T., Zhou, S. Y., Feng, Y. G., Ge, Z. X., Trujillo, A., … Liu, Z. (2012). Lithospheric and upper mantle structure of the northeastern Tibetan Plateau. *J. Geophys. Res. Solid Earth*, *117*(B5), B05307. https://doi.org/10.1029/2011JB008545

Zhang, G. B., Song, S. G., Zhang, L. F., and Niu, Y. L. (2008). The subducted oceanic crust within continental-type UHP metamorphic belt in the North Qaidam, NW China: Evidence from petrology, geochemistry and geochronology. *Lithos*, *104*(1–4), 99–118. https://doi.org/10.1016/j.lithos.2007.12.001

Zhang, J., Li, J. Y., Li, Y. F., and Ma, Z. J. (2007). The Cenozoic deformation of the Alxa block in central Asia-Question on the northeastern extension of the Altyn Tagh fault in Cenozoic time. *Acta Geol. Sin.* (*in Chinese*), *81*(11), 1481–1497. https://doi.org/10.3321/j.issn:0001-5717.2007.11.003

Zhang, J. X., Yu, S. Y., Li, Y. S., Yu, X. X., Lin, Y. H., and Mao, X. H. (2015). Subduction, accretion and closure of Proto-Tethyan Ocean: Early Paleozoic accretion/collision orogeny in the Altun-Qilian-North Qaidam orogenic system. *Acta Petrol. Sin.* (*in Chinese*), *31*(12), 3531–3554.

Zhang, P. Z., Shen, Z. K., Wang, M., Gan, W. J., Bürgmann, R., Molnar, P., Wang, Q., Niu, Z. J., Sun, J. Z., … You, X. Z. (2004). Continuous deformation of the Tibetan Plateau from Global Positioning System data. *Geology*, *32*(9), 809–812. https://doi.org/10.1130/G20554.1

Zhang, Q., Sandvol, E., Ni J., Yang, Y. J., and Chen, Y. J. (2011). Rayleigh wave tomography of the northeastern margin of the Tibetan Plateau. *Earth Planet. Sci. Lett.*, *304*(1–2), 103–112. https://doi.org/10.1016/j.epsl.2011.01.021

Zhang, Z. J., Bai, Z. M., Klemperer, S. L., Tian, X. B., Xu, T., Chen, Y., and Teng, J. W. (2013). Crustal structure across northeastern Tibet from wide-angle seismic profiling: Constraints on the Caledonian Qilian orogeny and its reactivation. *Tectonics*, *606*, 140–159. https://doi.org/10.1016/j.tecto.2013.02.040

Zheng W. J., Zhang P. Z., Ge W. P., Molnar P., Zhang H. P., Yuan D. Y., and Liu J. H. (2013). Late Quaternary slip rate of the South Heli Shan Fault (northern Hexi Corridor, NW China) and its implications for northeastward growth of the Tibetan Plateau. *Tectonics*, *32*, 271–293. https://doi.org/10.1002/tect.20022

Zheng, D., Li, H. Y., Shen, Y., Tan, J., Ouyang, L. B., and Li, X. F. (2016). Crustal and upper mantle structure beneath the northeastern Tibetan Plateau from joint analysis of receiver functions and Rayleigh wave dispersions. *Geophys. J. Int.*, *204*(1), 583–590. https://doi.org/10.1093/gji/ggv469

Zou, C. Q., He, R. Z., Duan, Y. H., Wei, Y. H., Liu, Q. X., and Liu, Y. (2017). Deep structure beneath the eastern Altyn Tagh fault and its vicinity derived from teleseismic P-wave tomography. *Chinese J. Geophys.* (*in Chinese*), *60*(6), 2279–2290. https://doi.org/10.6038/cjg20170620

Zuza, A. V., Cheng, X. G., and Yin, A. (2016). Testing models of Tibetan Plateau formation with Cenozoic shortening estimates across the Qilian Shan–Nan Shan thrust belt. *Geosphere*, *12*(2), 501–532. https://doi.org/10.1130/GES01254.1